



# The shape-controlled synthesis and novel lithium storage mechanism of as-prepared $\text{CuC}_2\text{O}_4 \cdot x\text{H}_2\text{O}$ nanostructures



Wenpei Kang, Qiang Shen\*

Key Laboratory for Colloid and Interface Chemistry of Education Ministry, School of Chemistry and Chemical Engineering, Shandong University, Jinan 250100, China

## HIGHLIGHTS

- $\text{CuC}_2\text{O}_4 \cdot x\text{H}_2\text{O}$  nanostructures are facilely obtained in the absence of additives.
- Structural properties of  $\text{CuC}_2\text{O}_4 \cdot x\text{H}_2\text{O}$  depend upon the polarity of reaction medium.
- A novel lithium storage mechanism of  $\text{CuC}_2\text{O}_4 \cdot x\text{H}_2\text{O}$  has been investigated.
- Crystal water induces an uptrend of  $\text{CuC}_2\text{O}_4 \cdot x\text{H}_2\text{O}$  reversible capacity on cycling.
- The 100th discharge capacity of  $\text{CuC}_2\text{O}_4 \cdot x\text{H}_2\text{O}$  reaches  $970 \text{ mAh g}^{-1}$  at  $200 \text{ mA g}^{-1}$ .

## ARTICLE INFO

### Article history:

Received 25 October 2012

Received in revised form

15 February 2013

Accepted 11 March 2013

Available online 25 March 2013

### Keywords:

Hydrate copper oxalate

Crystal water

Anode material

Lithium ion battery

## ABSTRACT

In a hydrothermal and solvothermal system at  $120^\circ\text{C}$ , cylinder-like and rod-like nanostructures of hydrate copper oxalate ( $\text{CuC}_2\text{O}_4 \cdot x\text{H}_2\text{O}$ ) can be thoroughly synthesized in the absence of any shape-controlling additives, respectively. The self-assembly of primary nanocrystals has been investigated considering the polarity of reaction medium, and in the chemical formula of  $\text{CuC}_2\text{O}_4 \cdot x\text{H}_2\text{O}$  the average  $x$  value of crystal water is estimated to discuss the superior lithium storage capability of hydrate products. The results show that cylinder-like aggregate of  $\text{CuC}_2\text{O}_4 \cdot x\text{H}_2\text{O}$  ( $x \sim 0.14$ ) possesses an initial discharge capacity of  $920.3 \text{ mAh g}^{-1}$  with a residual capacity of  $970.0 \text{ mAh g}^{-1}$  at  $200 \text{ mA g}^{-1}$  over 100 discharge–charge cycles, while rod-like aggregate with a  $x$  value of  $\sim 0.53$  per chemical formula exhibits a higher initial capacity of  $1211.3 \text{ mAh g}^{-1}$  and a lower retention of  $849.3 \text{ mAh g}^{-1}$  under the same conditions. Furthermore, time-dependent measurements present a novel crystal-to-amorphous transformation of active substances, suggesting a positive effect of unavoidable crystal water on the superior lithium storage capability of nanostructured  $\text{CuC}_2\text{O}_4 \cdot x\text{H}_2\text{O}$ .

© 2013 Elsevier B.V. All rights reserved.

## 1. Introduction

Facile synthesis, low cost, nanostructured feature and electrochemical reactivity are fashion trends of the research and development of electrode materials for lithium ion batteries (LIBs) with a high energy or power density. This is one of the main reasons why transition metal oxides have been tentatively used as active substances to replace conventional graphite as LIB anodes [1–4]. According to literature reports [5–10], dehydrated transition metal oxysalts can also be treated as conversion electrode materials for LIBs, especially, some of them can exhibit superior properties in comparison with their counterpart oxides. Therein, the adverse influence of water (i.e., moisture and/or crystal water) on the

electrochemical performance of oxysalts has already been eliminated prior to experiments. In some senses, transition metal oxysalts with a limited amount of unavoidable crystal water deserve to be conducted to assay their abnormal electrochemical behaviors under galvanostatic cycling conditions.

In fact, electrochemical reactions of a dehydrated oxalate during discharge–charge cycles have been simply described as: (i) the irreversible formation of solid electrolyte interface (SEI) in the first discharge process and (ii) the reciprocal conversion between transition metal and metal oxide thereafter [5–10]. The former explains the low initial coulomb efficiency, while the latter relates to the reversible lithium storage property of anhydrous phases. In an assembled lithium ion half-cell of dehydrated electrode materials, the unavoidable water contamination of moisture can induce the extra side reactions of water with  $\text{LiPF}_6$ -based electrolyte and lithium [11]. By contrast, crystal water in the chemical formula of electrode materials benefits the electrochemical crystal-to-amorphous transformation of

\* Corresponding author. Tel.: +86 531 88361387; fax: +86 531 88364464.  
E-mail address: [qshen@sdu.edu.cn](mailto:qshen@sdu.edu.cn) (Q. Shen).

active components [12,13]. Furthermore, crystal water could also enhance the electrochemical migration of Li-ions and then improve the cycling properties of hydrate materials.

Taking the experimental design of material preparation into consideration, transition metal oxysalts can be successfully synthesized using a reverse micelle procedure, and the involved micro-reactors of polar micelle core should satisfy the common criteria of nanofabrication [5–10]. To the best of our knowledge, anode materials with a specific nanostructured feature display distinguished physical and chemical properties to compare with the bulk ones. Especially, the structure-, shape- or size-dependent effectiveness has been well recognized as a crucial factor to overcome the drawbacks of LIB anode material, such as poor electronic conductivity, rapid capacity decay, etc [14–18]. In this case, shape-controlled synthesis of hydrate transition metal oxysalts should also be considered to highlight the influence of unavoidable crystal water on the possibly enhanced electrochemical properties of assembled LIBs.

In this paper, it is reported that cylinder-like or rod-like nanostructures of  $\text{CuC}_2\text{O}_4 \cdot x\text{H}_2\text{O}$  ( $0 < x < 1$ ) are thoroughly obtained from a hydrothermal or solvothermal precipitation reaction system in the absence of any morphological-controlling agents. Both the structural characteristics and electrochemical properties of crystalline  $\text{CuC}_2\text{O}_4 \cdot x\text{H}_2\text{O}$  (i.e., hydro- or solvo-thermal product) and the involved structure–function relationships are the main topics of this paper. By comparison with the electrochemical properties of other dehydrated oxysalts and CuO-based anode materials reported in literature, the presence of unavoidable crystal water and its positive effect on the observed superior lithium storage capability of different  $\text{CuC}_2\text{O}_4 \cdot x\text{H}_2\text{O}$  nanostructures are systematically investigated for the first time.

## 2. Experimental

### 2.1. Synthesis of $\text{CuC}_2\text{O}_4 \cdot x\text{H}_2\text{O}$

All chemicals are of analytical grade and were used as received.  $\text{CuC}_2\text{O}_4 \cdot x\text{H}_2\text{O}$  crystals were facily obtained from an aqueous solution (40 mL, 120 °C) in the absence and presence of 30 mL ethyl glycol (EG), and the resulting products were defined as hydro- or solvo- $\text{CuC}_2\text{O}_4 \cdot x\text{H}_2\text{O}$ , respectively. Typically, 5 mmol  $\text{CuCl}_2$  (s) was dissolved into 40 mL deionized water (or, 30 mL EG + 10 mL deionized water) and then 5 mmol  $\text{H}_2\text{C}_2\text{O}_4$  (s) was added under a vigorous magnetic stirring for 0.5 h. Subsequently, the resulting suspension was transferred into a 100-mL Teflon-lined stainless steel autoclave, allowed to stand still in a 120 °C thermostatic chamber for 12 h. Finally, the autoclave was cooled down to room temperature, and the hydro- or solvo- $\text{CuC}_2\text{O}_4 \cdot x\text{H}_2\text{O}$  was collected by centrifugation, washed with deionized water and then ethanol for 3 times, and dried in a 120 °C vacuum desiccator for 24 h.

### 2.2. Structure characterization

X-ray diffraction (XRD) data were collected on a Rigaku D/max-2400 powder X-ray diffractometer with Cu K $\alpha$  radiation (40 kV, 120 mA) in the  $2\theta$  range of 10–80°. Both the hydro- and solvo- $\text{CuC}_2\text{O}_4 \cdot x\text{H}_2\text{O}$  samples were Pt-coated prior to examination by a JEOL JSM-6700F scanning electron microscope (SEM), fitted with a field emission source and operating at an accelerating voltage of 15 kV. The as-prepared samples were dispersed in ethanol by ultrasonication and then deposited on a carbon film supported by the copper grid, prior to low- and high-resolution transmission electron microscopy (TEM and HR TEM) measurements on a JEM 2100 microscope (200 kV). Thermogravimetric analyzer (TGA) measurement was performed under air atmosphere with a heating

step of 10 °C min<sup>−1</sup> from room temperature to 800 °C. X-ray photoelectron spectra (XPS) measurements were performed on ESCALAB 250 X-ray photoelectron spectrometer.

### 2.3. Electrochemical characterization

The working electrode was prepared using the mixture of  $\text{CuC}_2\text{O}_4 \cdot x\text{H}_2\text{O}$ , acetylene black and sodium alginate at a weight ratio of 70:20:10. Lithium metal, nickel foam, glass fibers and commercial LBC 305-01  $\text{LiPF}_6$  solution (Shenzhen Xinzhoubang) were used as counter electrode, current collector, separator and electrolyte, respectively. CR2032-type coin cells were assembled in an argon-filled glove box. Galvanostatic cycling tests were measured on LAND CT2001A system (Wuhan Landian) in the voltage range of 0.01–3.0 V (vs.  $\text{Li}^+/\text{Li}$ ). Cyclic voltammetry (CV) curves were obtained on an LK 2005A Electrochemical Workstation (Tianjin Lanlike) at 0.1 mV s<sup>−1</sup> in the voltage range of 0.0–3.0 V (vs.  $\text{Li}^+/\text{Li}$ ). To investigate the reaction mechanism of  $\text{CuC}_2\text{O}_4 \cdot x\text{H}_2\text{O}$  with lithium, galvanostatic cycling tests were stopped and coin cells were unpacked in an air–atmosphere ventilating cabinet. Therein, the active substances of working electrode were washed with ethanol for 3 times, dried at 100 °C, and then used for XRD and XPS measurements.

## 3. Results and discussion

As shown in Fig. 1a, XRD patterns of as-prepared samples coincide well with the standard data of orthorhombic  $\text{CuC}_2\text{O}_4 \cdot x\text{H}_2\text{O}$  crystals ( $0 < x < 1$ ) (JCPDS 21-0297). Therein, the width of each

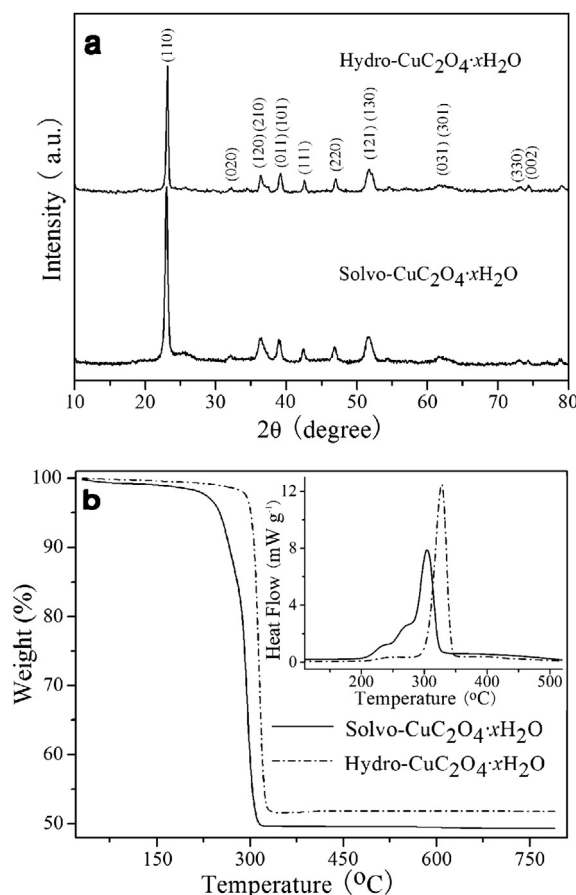


Fig. 1. (a) XRD and (b) TGA patterns of hydro- and solvo- $\text{CuC}_2\text{O}_4 \cdot x\text{H}_2\text{O}$ , and the inset in panel (b) is corresponding DSC curves.

diffraction peaks is relatively broad, indicating that the average size of primary particles is at nanoscale. According to the full-width at half maximum (FWHM) of (110) crystal plane, the calculated interplanar spacing of (110) face can be treated as an equivalent for the average size of primary nanocrystals, giving a value of 19.1 and 26.7 nm for hydro- and solvo- $\text{CuC}_2\text{O}_4 \cdot x\text{H}_2\text{O}$ , respectively. Fig. 1b presents the comparative TGA curves of these hydrate products, confirming the simultaneous dehydration and decomposition of  $\text{CuC}_2\text{O}_4 \cdot x\text{H}_2\text{O}$  under air atmosphere [19]. As shown in equation (1), even at a dehydration temperature around 200 °C, a long-time heat treatment still results in black copper (II) oxide (CuO), indicating the structural stability of crystalline  $\text{CuC}_2\text{O}_4 \cdot x\text{H}_2\text{O}$  prior to its transfer to an assembled  $\text{CuC}_2\text{O}_4 \cdot x\text{H}_2\text{O}/\text{Li}$  half-cell.



From the inset in Fig. 1b, the thermal dehydration and oxygen-assisted decomposition of crystalline  $\text{CuC}_2\text{O}_4 \cdot x\text{H}_2\text{O}$  occur at ca. 250 and 320 °C, respectively. Although it is difficult to obviously distinguish one from the other at a heating step of 10 °C min<sup>-1</sup>, according to the total weight loss of 48.2% and 50.5% for hydro- and solvo- $\text{CuC}_2\text{O}_4 \cdot x\text{H}_2\text{O}$ , the corresponding  $x$  values of 0.14 and 0.53 are estimated, respectively.

On the basis of Jongen's opinions [20], a crystal plane of copper oxalate possesses a relatively hydrophobic or hydrophilic nature in lattice structures. This is the reason why the as-prepared hydrothermal or solvothermal products present a defined value of crystal water

per formula. Similarly for adjacent nanocrystals, the hydrophobic interactions among the manifest hydrophobic crystal faces interpret a facile formation of ribbon- or rod-like two-dimensional nanostructures of crystalline  $\text{CuC}_2\text{O}_4 \cdot x\text{H}_2\text{O}$  [20–22]. Herein, SEM observation displays that as-prepared hydro- $\text{CuC}_2\text{O}_4 \cdot x\text{H}_2\text{O}$  is the cylinder-like architecture composed of an ordered array of nanorods (Fig. 2a,b). Perhaps, a mesoscale self-assembly for the generation of three-dimensional nanostructures still originates from the so-called hydrophobic interparticle interactions among the already-formed hydro- $\text{CuC}_2\text{O}_4 \cdot x\text{H}_2\text{O}$  nanorods in a polar reaction medium.

A representative TEM image shows that the occasionally captured secondary nanorods are the aggregates of tiny nanoparticles (Fig. 2c). In Fig. 2c, the inserted TEM picture corresponds to an overview for the three-dimensional cylinder-like nanostructures of hydro- $\text{CuC}_2\text{O}_4 \cdot x\text{H}_2\text{O}$ . It should be mentioned that the microstructure of a rod-like component is well consistent with that of  $\text{CuC}_2\text{O}_4 \cdot x\text{H}_2\text{O}$  rods described in Ref. [22]. However, selective area electrode diffraction (SAED) technique can hardly be used to determine the crystallinity of these nanoparticles, because of the high instability of nanocrystalline  $\text{CuC}_2\text{O}_4 \cdot x\text{H}_2\text{O}$  under the irradiation of electron beam [20]. Nevertheless, by focusing electron beam on a nanorod, HR TEM observation sometimes presents the existence of crystalline nanodomains marked by dash circles (Fig. 2d). What's more, the ambiguous lattice fringes within a nanodomain are magnified and shown as an inset in Fig. 2d.

By comparison, the polarity of the mixture of EG and water at a volume ratio of 3:1 is weaker than that of deionized water. This indicates that hydrophobic crystal planes of primarily formed

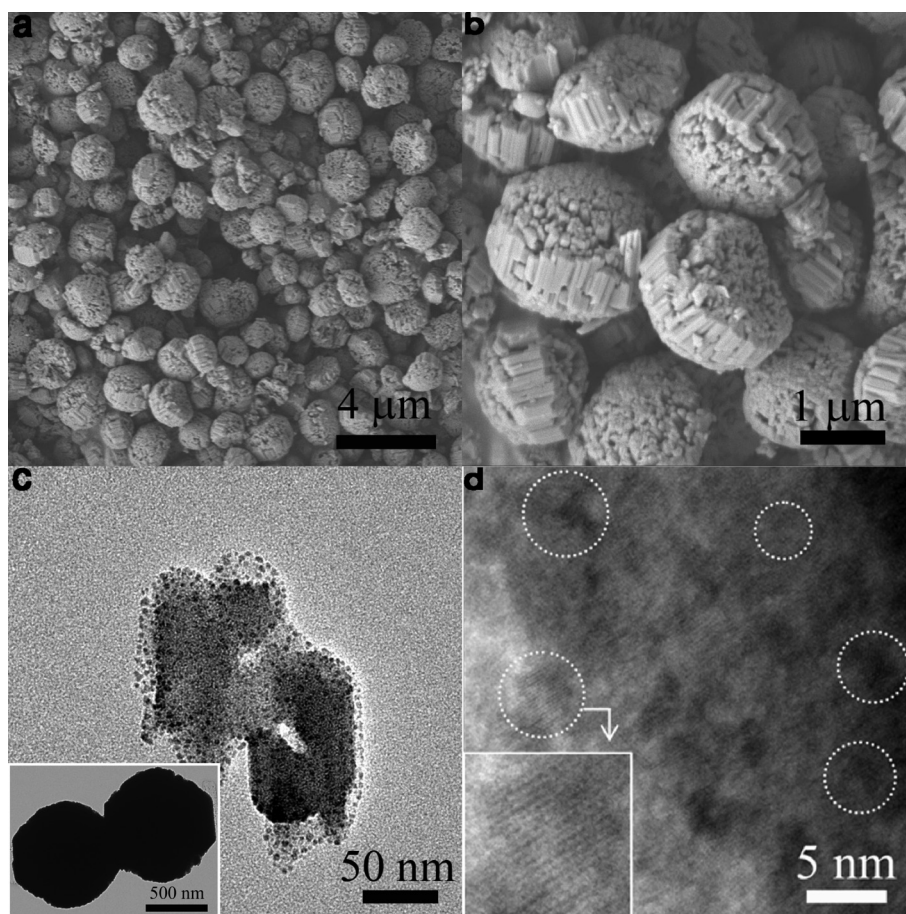


**Fig. 2.** (a, b) SEM, (c) TEM and (d) HR TEM images for hydro- $\text{CuC}_2\text{O}_4 \cdot x\text{H}_2\text{O}$ . Panel (c) shows a TEM picture of rod-like components, while the inset corresponds to that of cylinder-like aggregates. In panel (d), dash circles denote crystalline nanodomains within a nanorod, and inset is the corresponding lattice fringes of a representative nanodomain.



$\text{CuC}_2\text{O}_4 \cdot x\text{H}_2\text{O}$  can be occupied by a relatively much amount of weak polar solvents [20–25]. Therefore, solvothermal reaction merely results in two-dimensional rod-like configurations of solvo- $\text{CuC}_2\text{O}_4 \cdot x\text{H}_2\text{O}$  with the relatively big  $x$  value of  $\sim 0.53$  per chemical formula (Fig. 3a). By statistic analysis, these as-obtained nanorods give an average length of  $107.1 \pm 26.4$  nm and an aspect ratio of  $\sim 5.1$ . Overview and close-up view of TEM pictures show that solvo- $\text{CuC}_2\text{O}_4 \cdot x\text{H}_2\text{O}$  products are the rod-like aggregates of tiny nanoparticles with an average size of several nanometers (Fig. 3b–d). Resembling the crystallinity of hydro- $\text{CuC}_2\text{O}_4 \cdot x\text{H}_2\text{O}$  building blocks, the as-prepared solvo- $\text{CuC}_2\text{O}_4 \cdot x\text{H}_2\text{O}$  can occasionally exhibit a nanoparticle with the lattice fringes of orthorhombic structure, shown as an inset in Fig. 3d.

Interestingly, under an argon atmosphere, 24-h immersion in  $\text{LiPF}_6$ -based electrolyte exerts almost no influence on the lattice structure of crystalline  $\text{CuC}_2\text{O}_4 \cdot x\text{H}_2\text{O}$ , which presents the same XRD patterns as those shown in Fig. 1a. This means that: (i) there is no direct reaction between crystal water and  $\text{LiPF}_6$ -based electrolyte; (ii) in assembled  $\text{CuC}_2\text{O}_4 \cdot x\text{H}_2\text{O}/\text{Li}$  half-cells, the possible adverse or beneficial effectiveness of crystal water may occur owing to the electrochemical destroying of crystalline  $\text{CuC}_2\text{O}_4 \cdot x\text{H}_2\text{O}$  by the simultaneous release of water molecules.

Within the potential range of 0.01–3.0 V, discharge–charge profiles of hydro- and solvo- $\text{CuC}_2\text{O}_4 \cdot x\text{H}_2\text{O}$  are shown in Fig. 4. For a hydro- $\text{CuC}_2\text{O}_4 \cdot x\text{H}_2\text{O}$  ( $x \sim 0.14$ ) electrode, its initial discharge capacity is  $920.3 \text{ mAh g}^{-1}$ , while the corresponding charge capacity is only  $397.1 \text{ mAh g}^{-1}$  (Fig. 4a). The ultra low value of initial Coulomb efficiency (43.1%) is attributed to irreversible side reactions, including the electrochemical release of crystal water and the

formation of solid electrolyte interface (SEI) films [26,27]. Subsequently, the obviously gradual decay of discharge capacity for the first 4 full-cycles proves that the presence of crystal water should exert an unsatisfactory influence on the lithium storage capability [5–10]. Surprisingly, thereafter the hydro- $\text{CuC}_2\text{O}_4 \cdot x\text{H}_2\text{O}$  displays the 10th, 50th and 100th discharge capacities of 612.1, 833.3 and  $970.0 \text{ mAh g}^{-1}$  at a current density of  $200 \text{ mA g}^{-1}$ , and each reversible cycle gives a high Coulomb efficiency around 98.5% (Fig. 4b). Therefore, a beneficial effectiveness of crystal water should exist in contrast with the initially unsatisfactory influence during the first 4 cycles, which is nearly consistent with C. Pérez Vicente's results of  $\text{CuC}_2\text{O}_4 \cdot 0.5\text{H}_2\text{O}$  reported recently [19].

In comparison with the electrochemical data shown in Fig. 4a and b, solvo- $\text{CuC}_2\text{O}_4 \cdot x\text{H}_2\text{O}$  ( $x \sim 0.53$ ) electrode displays a higher initial discharge capacity of  $1211.3 \text{ mAh g}^{-1}$  with a lower initial Coulomb efficiency of 42.0%, which can be assigned to the relatively high amount of crystal water per chemical formula. Similarly after the first 4 cycles, a recovery for the lithium storage capability of solvo- $\text{CuC}_2\text{O}_4 \cdot x\text{H}_2\text{O}$  is relatively low, giving the 10th, 50th and 100th specific discharge capacity of 626.3, 627.9 and  $849.3 \text{ mAh g}^{-1}$ , respectively (Fig. 4c,d). Both the initial and 100th discharge capacities of hydro- and solvo- $\text{CuC}_2\text{O}_4 \cdot x\text{H}_2\text{O}$  electrodes are much higher than the theoretical value of commercially used graphite ( $372 \text{ mAh g}^{-1}$ ), anyway, the large initial capacity loss (e.g., solvo- $\text{CuC}_2\text{O}_4 \cdot x\text{H}_2\text{O} \sim 58.0\%$ ) in the first cycle should be greatly restrained for a potential applicability. Herein, we would like to cite the relative solutions reported recently: a simple pre-lithiation of active substances or their complexation with  $\text{Li}_2\text{O}$  [28,29]. In some senses, high-capacity  $\text{CuC}_2\text{O}_4 \cdot x\text{H}_2\text{O}$  deserves to be further conducted, and

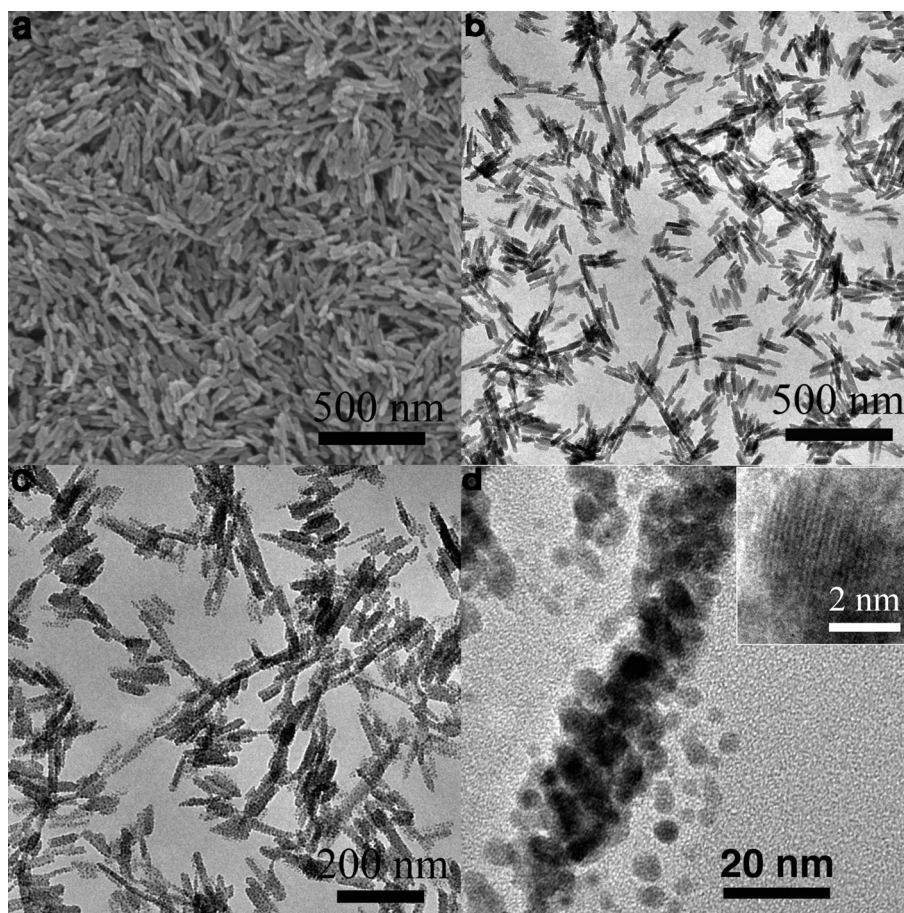


Fig. 3. (a) SEM and (b–d) TEM images for solvo- $\text{CuC}_2\text{O}_4 \cdot x\text{H}_2\text{O}$ . Inset is the corresponding lattice fringes of a representative nanoparticle.

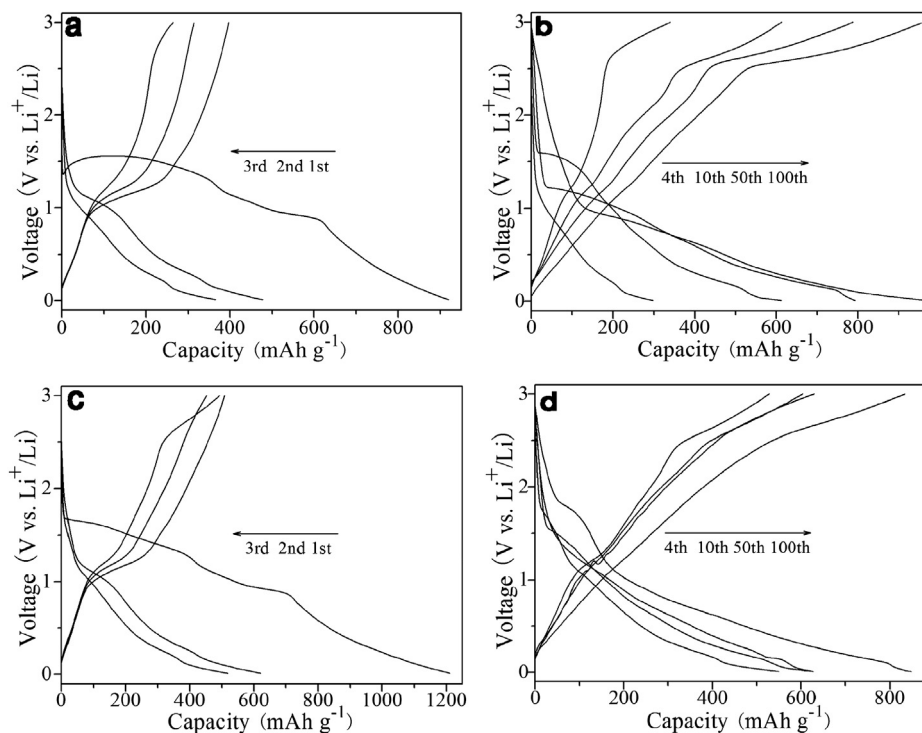


Fig. 4. Discharge–charge profiles of (a, b) hydro- and (c, d) solvo- $\text{Cu}_2\text{O}_4 \cdot x\text{H}_2\text{O}$  electrodes operated at  $200 \text{ mA g}^{-1}$ .

the simple pretreatments may eliminate the initial adverse effect of released crystal water.

In order to fully understand the cycling stability and rate-cycling performances of hydro- and solvo- $\text{Cu}_2\text{O}_4 \cdot x\text{H}_2\text{O}$ , the plots of specific discharge capacity against cycle number at a current density of 200 or  $500 \text{ mA g}^{-1}$  are shown in Fig. 5. At each discharge–charge current density, both hydro- and solvo- $\text{Cu}_2\text{O}_4 \cdot x\text{H}_2\text{O}$  electrodes experience an initial decrease in discharge capacity and then a successive increase thereafter. By comparison with rod-like solvo- $\text{Cu}_2\text{O}_4 \cdot x\text{H}_2\text{O}$  ( $x \sim 0.53$ ) cycled at 200 or  $500 \text{ mA g}^{-1}$ , cylinder-like hydro- $\text{Cu}_2\text{O}_4 \cdot x\text{H}_2\text{O}$  ( $x \sim 0.14$ ) nanostructures display a lower initial discharge capacity, a bigger capacity decay for the initial several cycles, thereafter, a bigger capacity increase subsequently and a higher capacity retention over 100 cycles.

In Fig. 5, at each current density, the lower initial discharge capacity and higher capacity retention of hydro- $\text{Cu}_2\text{O}_4 \cdot x\text{H}_2\text{O}$

( $x \sim 0.14$ ) seem to be reasonably interpreted by the less amount of unavoidable crystal water per chemical formula, however, these do conflict with its lower value of the minimum extreme therein. Moreover, even at a higher current rate of  $500 \text{ mA g}^{-1}$ , the 100th discharge capacities of hydro- and solvo- $\text{Cu}_2\text{O}_4 \cdot x\text{H}_2\text{O}$  are still higher than that of commercially used graphite (i.e.,  $372 \text{ mAh g}^{-1}$ ), attaining a value of 809.5 and  $687.8 \text{ mAh g}^{-1}$ , respectively.

To neglect an initially negative influence of crystal water on the capacity decay of  $\text{Cu}_2\text{O}_4 \cdot x\text{H}_2\text{O}$  electrodes, it is of great scientific interests to clarify the relationship between unavoidable crystal water and superior lithium storage capability, based on the following aspects. (i) According to equation (1), even if high-capacity CuO can merely be recognized as an intermediate of electrochemically cycled  $\text{Cu}_2\text{O}_4 \cdot x\text{H}_2\text{O}$ , the 100th discharge capacity of hydrate copper oxalate (e.g.,  $970.0 \text{ mAh g}^{-1}$ ) is still higher than the theoretical capacity of CuO (i.e.,  $674.0 \text{ mAh g}^{-1}$ ). (ii) By comparison with the literature results of CuO/C summarized in Table 1 [30–33], the lithium storage capability of hydro- or solvo- $\text{Cu}_2\text{O}_4 \cdot x\text{H}_2\text{O}$  is also very high, indicating a novel lithium storage mechanism therein.

It has been reported that an irreversible crystal-to-amorphous transformation for the first discharge half-cycle and a subsequently reversible conversion between amorphous oxides and corresponding transition metal account for the electrochemical properties of dehydrated metal oxalates [5]. Also, for a composite anode of quantum-dot transition metal oxides, it is the conductivity increase (i.e., not the amorphization) of active substances that determines the upward trends of discharge capacity during continuous discharge–charge cycles [34]. Inspired by these, the beneficial influence of unavoidable crystal water on the initial formation of amorphous  $\text{Cu}^{2+}$ -based intermediates should be hypothesized, according to time-dependent experimental results shown below.

For a solvo- $\text{Cu}_2\text{O}_4 \cdot x\text{H}_2\text{O}$  electrode in the 1st cathodic process, the wide CV peak in a voltage range of 1.85–1.15 V can be attributed

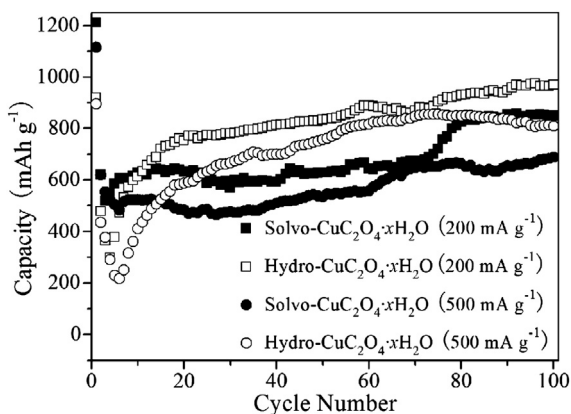


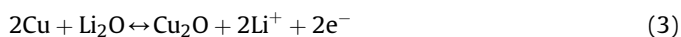
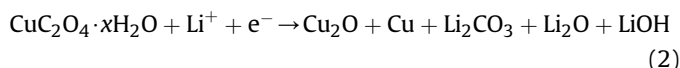
Fig. 5. Cycling performances of nanostructured  $\text{Cu}_2\text{O}_4 \cdot x\text{H}_2\text{O}$  measured at different current rate.

**Table 1**A summary for the lithium storage capability of as-prepared  $\text{CuC}_2\text{O}_4 \cdot x\text{H}_2\text{O}$  nanostructures, dehydrated oxysalts and CuO-based anode materials reported previously.

| Material   | Shape/size  | Residual capacity<br>(mAh g <sup>-1</sup> ) | Current or C <sup>a</sup> | Ref.      |
|--|---|---|---------------------------|-----------|
| $\text{CuC}_2\text{O}_4 \cdot x\text{H}_2\text{O}$ | Cylinder-like shape/ $\sim 2 \mu\text{m}$ in diameter | 970.0/100th cycle                           | 200 mA g <sup>-1</sup>    | This work |
| $\text{CuC}_2\text{O}_4 \cdot x\text{H}_2\text{O}$ | Rod-like shape/ $\sim 107 \text{ nm}$ in length       | 809.5/100th cycle                           | 500 mA g <sup>-1</sup>    | This work |
| $\text{MnCO}_3$                                    | Rhombohedral/200 nm                                   | 849.3/100th cycle                           | 200 mA g <sup>-1</sup>    | [5]       |
| $\text{FeC}_2\text{O}_4$                           | Elongated-shape/150 nm in width                       | 687.8/100th cycle                           | 500 mA g <sup>-1</sup>    | [6]       |
| $\text{CoC}_2\text{O}_4$                           | Nanoribbon/30 nm in width                             | >466/25th cycle                             | 2C                        | [9]       |
| CuO  | Urchin-like shape/200 nm                              | >400/75th cycle                             | 2C                        | [18]      |
| CuO/C  | Microsphere/2 $\mu\text{m}$                           | >560/50th cycle                             | 150 mA g <sup>-1</sup>    | [28]      |
| CNT/CuO  | Microsphere/2.5 $\mu\text{m}$                         | 470/50th cycle                              | 100 mA g <sup>-1</sup>    | [29]      |
| CuO/graphene                                       | Granule/30 nm   | 500/25th cycle                              | 67 mA g <sup>-1</sup>     | [30]      |
| CuO  | Nanoparticle/30 nm                                    | 583.5/50th cycle                            | 67 mA g <sup>-1</sup>     | [31]      |
|  |   | 665.8/100th cycle                           | 1348 mA g <sup>-1</sup>   |           |

<sup>a</sup> C = 1 Li h<sup>-1</sup> mol<sup>-1</sup>.

to the complete consumption of crystal water once for all, also including the amorphization of dehydrated oxalates and the formation of SEI films [26,27]. This assignment is made because the subsequent peak around 0.85 V coincides well with the reduction of amorphous copper oxalate [10]. Furthermore, there is only one peak appearing around 1.28 V in the 1st anodic half-cycle, corresponding to the oxidation of amorphous intermediates (Fig. 6a). The initial reaction of  $\text{CuC}_2\text{O}_4 \cdot x\text{H}_2\text{O}$  with lithium can be briefly expressed as equation (2) listed below.

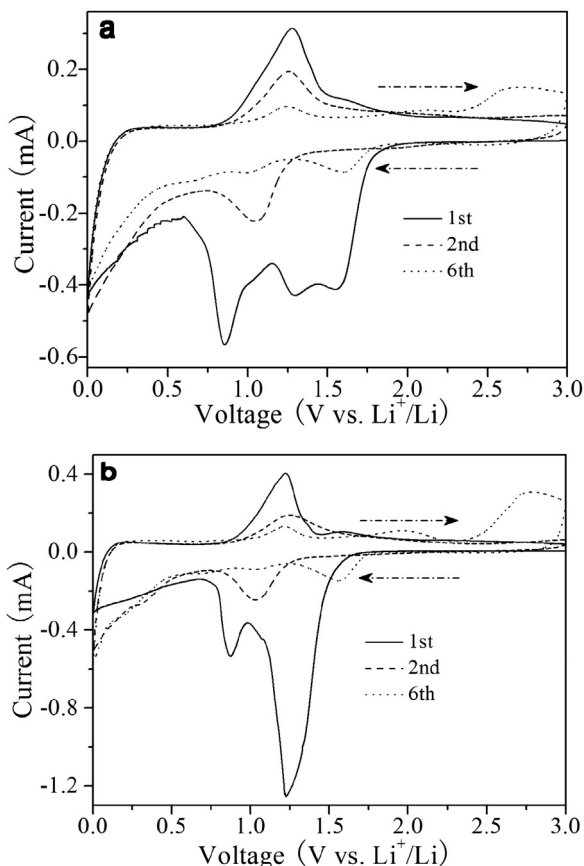


For the 2nd full-cycle shown in Fig. 6a, a cathodic peak around 1.05 V and an anodic peak around 1.28 V correspond to the redox reaction between  $\text{Cu}_2\text{O}$  and Cu, described as equation (3). Afterward, another couple of reduction and oxidation peaks appear at  $\sim 1.7$  and 2.65 V in the 6th discharge–charge cycle, respectively, and the intensities of which increase gradually upon the further cycling (Fig. 6a). On the principle of electrode potential, this novel redox reaction can be assigned to the reversible conversion reaction of  $\text{Cu}_2\text{O}$  and  $\text{Li}_2\text{CuO}_2$ , shown in equation (4) [35,36].

Fig. 6b presents CV behaviors of a hydro- $\text{CuC}_2\text{O}_4 \cdot x\text{H}_2\text{O}$  ( $x \sim 0.14$ ) electrode, which indicates almost the same lithium storage mechanism as that of solvo- $\text{CuC}_2\text{O}_4 \cdot x\text{H}_2\text{O}$  ( $x \sim 0.53$ ). The only difference is that an amazing peak at  $\sim 2.00$  V obviously appears for the oxidation reaction of  $\text{Cu}_2\text{O}$  into CuO in the 6th anodic process of hydro- $\text{CuC}_2\text{O}_4 \cdot x\text{H}_2\text{O}$  (Fig. 6b). Therefore, the presence of crystal water in lattice structures induces the initial amorphization of  $\text{CuC}_2\text{O}_4 \cdot x\text{H}_2\text{O}$ , subsequently promotes the reversible conversion between metal Cu and copper oxides and finally causes the gradual formation of active  $\text{Li}_2\text{CuO}_2$  [34,35]. Most importantly, these could be proved by the crystal phase determination of electrochemical reaction products collected at different intervals (Fig. 7a).

As shown in ex-situ XRD patterns (Fig. 7a), there is the sharp weakening of reflection intensity for metal Cu after the 1st charge process, also the obvious detection of  $\text{Li}_2\text{CuO}_2$  after the 6th or 100th cathodic half-cycles. Therefore, the gradually accumulated Cu,  $\text{Cu}_2\text{O}$  and  $\text{Li}_2\text{CuO}_2$ , as well as the reversible reactions between them, explain the anomalous capacity increase shown in Fig. 5.

The X-ray photoelectron spectra of Cu 2p for pristine  $\text{CuC}_2\text{O}_4 \cdot x\text{H}_2\text{O}$  and its electrochemical reaction intermediates are shown in Fig. 7b or c. For analysis purposes, two aspects should be emphasized: (i) binding energy shift is difficult to distinguish the valence of copper (i.e.,  $\text{Cu}^0$ ,  $\text{Cu}^{1+}$ ,  $\text{Cu}^{2+}$  and  $\text{Cu}^{3+}$ ) and (ii) Cu 2p<sub>3/2</sub> peak and its shake-up satellites are uniquely indicative of the divalent compounds. From Fig. 7b, there are strong Cu 2p<sub>3/2</sub> shake-up satellites for pristine  $\text{CuC}_2\text{O}_4 \cdot x\text{H}_2\text{O}$  and relatively weak ones for the 1st discharged samples. And then, the subsequently incomplete and irreversible transformation of amorphous  $\text{Cu}^{2+}$ -intermediates to Cu and  $\text{Cu}_2\text{O}$  interprets the appearance of  $\text{Cu}^{2+}$ -compounds' XPS characteristics even after the 100th discharge half-cycle (Fig. 7c).

**Fig. 6.** CV curves of (a) solvo- and (b) hydro- $\text{CuC}_2\text{O}_4 \cdot x\text{H}_2\text{O}$  scanned at 0.1 mV s<sup>-1</sup>.



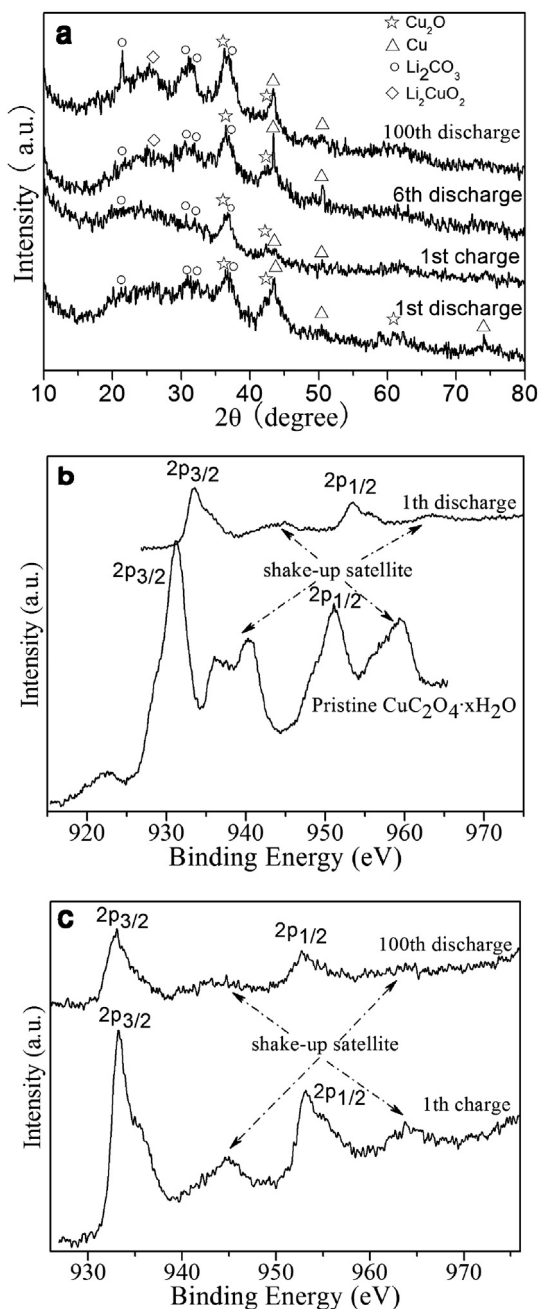


**Fig. 7.** (a) XRD patterns of the electrochemically cycled  $\text{CuC}_2\text{O}_4 \cdot x\text{H}_2\text{O}$  sampled at different reaction intervals; (b, c) XPS spectra of Cu 2p for reactant  $\text{CuC}_2\text{O}_4 \cdot x\text{H}_2\text{O}$  and its electrochemical cycled products.

#### 4. Conclusions

In summary, cylinder-like or rod-like  $\text{CuC}_2\text{O}_4 \cdot x\text{H}_2\text{O}$  nanostructures can be facilely synthesized from a hydrothermal or solvothermal system in the absence of any shape-controlling agents, and the hydrophobic interactions among hydrophobic crystal planes of copper oxalate accounts for the self-assembly of tiny nanoparticles therein. Especially, a hierarchically ordered feature of nanostructured  $\text{CuC}_2\text{O}_4 \cdot x\text{H}_2\text{O}$  and the involved  $x$  value in each chemical formula are different, owing to the polarity difference of reaction medium. When tentatively applied as LIB anodes, cylinder-like hydro- $\text{CuC}_2\text{O}_4 \cdot x\text{H}_2\text{O}$  ( $x \sim 0.14$ ) gives a superior lithium storage capability, attaining the 100th specific discharge capacity of 970.0

and 809.5  $\text{mAh g}^{-1}$  at a current density of 200 and 500  $\text{mA g}^{-1}$ , respectively. Similarly, rod-like solvo- $\text{CuC}_2\text{O}_4 \cdot x\text{H}_2\text{O}$  ( $x \sim 0.53$ ) can also achieve the 100th specific discharge capacities of 849.3 and 687.8  $\text{mAh g}^{-1}$  under the same experimental conditions. The presence of crystal water causes a rapid decrease of discharge capacity in the initial several discharge–charge cycles, which surprisingly induces the gradual formation of newly active  $\text{Li}_2\text{CuO}_2$  for subsequent cycles. To a great extent, this novel lithium storage mechanism explains the observed anomalous capacity increase of  $\text{CuC}_2\text{O}_4 \cdot x\text{H}_2\text{O}$  upon cycling, however, the restraint of irreversible capacity in the initial cycles needs to be further conducted in future.

#### Acknowledgments

The authors thank the financial supports from Shandong Province (ZR2012BM001), from the National Basic Research Program of China (2011CB935900) and from the NCET Program in University.

#### References

- [1] F.Y. Cheng, J. Liang, Z.L. Tao, J. Chen, *Adv. Mater.* 23 (2011) 1695–1715.
- [2] V. Etacheri, R. Marom, R. Elazari, G. Salitra, D. Aurbach, *Energy Environ. Sci.* 4 (2011) 3243–3262.
- [3] L.W. Ji, Z. Lin, M. Alcoutlabi, X.W. Zhang, *Energy Environ. Sci.* 4 (2011) 2682–2699.
- [4] Y.G. Wang, H.Q. Li, P. He, E. Hosono, H.S. Zhou, *Nanoscale* 2 (2010) 1294–1305.
- [5] M.J. Aragón, C. Perez-Vicente, J.L. Tirado, *Electrochem. Commun.* 9 (2007) 1744–1748.
- [6] M.J. Aragón, B. León, C.P. Vicente, J.L. Tirado, *Inorg. Chem.* 47 (2008) 10366–10371.
- [7] M.J. Aragón, B. León, C.P. Vicente, J.L. Tirado, *J. Power Sources* 189 (2009) 823–827.
- [8] M.J. Aragón, B. León, T. Serrano, C. Perez-Vicente, J.L. Tirado, *J. Mater. Chem.* 21 (2011) 10102–10107.
- [9] M.J. Aragón, B. León, C.P. Vicente, J.L. Tirado, *Chem. Mater.* 21 (2009) 1834–1840.
- [10] F. Nacimiento, R. Alcántara, J.L. Tirado, *J. Electroanal. Chem.* 642 (2010) 143–149.
- [11] D. Aurbach, I. Weissman, A. Zaban, P. Dan, *Electrochim. Acta* 45 (1999) 1135–1140.
- [12] S. Bach, J.P. Pereira-Ramos, N. Baffier, *Solid State Ionics* 80 (1995) 151–158.
- [13] R. Xu, J.R. Li, A. Tan, Z.L. Tang, Z.G. Zhang, *J. Power Sources* 196 (2011) 2283–2288.
- [14] J.Y. Xiang, J.P. Tu, L. Zhang, Y. Zhou, X.L. Wang, S.J. Shi, *J. Power Sources* 195 (2010) 313–319.
- [15] W.P. Kang, F.L. Liu, Y.L. Su, D.J. Wang, Q. Shen, *CrystEngComm* 13 (2011) 4174–4180.
- [16] J.S. Chen, L.A. Archer, X.W. Lou, *J. Mater. Chem.* 21 (2011) 9912–9924.
- [17] X.P. Gao, J.L. Bao, G.L. Pan, H.Y. Zhu, P.X. Huang, F. Wu, D.Y. Song, *J. Phys. Chem. B* 108 (2004) 5547–5551.
- [18] J.C. Park, J. Kim, H. Kwon, H. Song, *Adv. Mater.* 21 (2009) 803–807.
- [19] M.C. López, J.L. Tirado, C.P. Vicente, *J. Power Sources* 227 (2013) 65–71.
- [20] N. Jongen, P. Bowen, J. Lemaitre, J.-C. Valmalette, H. Hofmann, *J. Colloid Interface Sci.* 226 (2000) 189–198.
- [21] J. Romann, J.-C. Valmalette, V. Chevallier, A. Merlen, *J. Phys. Chem. C* 114 (2010) 10677–10682.
- [22] R. Ranjan, S. Vaidya, P. Thapliyal, M. Qamar, J. Ahmed, A.K. Ganguli, *Langmuir* 25 (2009) 6469–6475.
- [23] W.P. Kang, C.H. Zhao, R. Liu, F.F. Xu, Q. Shen, *CrystEngComm* 14 (2012) 2245–2250.
- [24] X.Y. Yu, R.X. Xu, C. Gao, T. Luo, Y. Jia, J.H. Liu, X.J. Huang, *ACS Appl. Mater. Interfaces* 4 (2012) 1954–1962.
- [25] Q. Xiao, *Powder Technol.* 189 (2009) 103–107.
- [26] X.X. Li, F.Y. Cheng, S.N. Zhang, J. Chen, *J. Power Sources* 160 (2006) 542–547.
- [27] K. Saravanan, M. Nagarathinam, P. Balaya, J.J. Vittal, *J. Mater. Chem.* 20 (2010) 8329–8335.
- [28] J. Hassoun, K.S. Lee, Y.K. Sun, B. Scrosati, *J. Am. Chem. Soc.* 133 (2011) 3139–3143.
- [29] Y. Yu, C.-H. Chen, J.-L. Shui, S. Xie, *Angew. Chem. Int. Ed.* 44 (2005) 7085–7089.
- [30] X.H. Huang, C.B. Wang, S.Y. Zhang, F. Zhou, *Electrochim. Acta* 56 (2011) 6752–6756.
- [31] S.F. Zheng, J.S. Hu, L.S. Zhong, W.G. Song, L.J. Wan, Y.G. Guo, *Chem. Mater.* 20 (2008) 3617–3622.
- [32] Y.J. Mai, X.L. Wang, J.Y. Xiang, Y.Q. Qiao, D. Zhang, C.D. Gu, J.P. Tu, *Electrochim. Acta* 56 (2011) 2306–2311.
- [33] W.P. Kang, C.H. Zhao, Q. Shen, *Int. J. Electrochem. Sci.* 7 (2012) 8194–8204.
- [34] C.X. Peng, B.D. Chen, Y. Qin, S.H. Yang, C.Z. Li, Y.H. Zuo, S.Y. Liu, J.H. Yang, *ACS Nano* 6 (2012) 1074–1081.
- [35] T. Li, X.P. Ai, H.X. Yang, *J. Phys. Chem. C* 115 (2011) 6167–6174.
- [36] G. Vitins, E.A. Raekelboom, M.T. Weller, J.R. Owen, *J. Power Sources* 119–121 (2003) 938–942.